The petrogenesis of orbicular granites in the Diana's Pool area, Zimbabwe

S.S. Dumisa
School of Geosciences, University of the Witwatersrand, 1 Jan Smuts Avenue, Braamfontein 2000, Johannesburg, South Africa
Current address; Department of Geology, University of Johannesburg, Corner Kingsway, University Road, Johannesburg, 2092, South Africa
e-mail: senamiled@uj.ac.za,869622@students.wits.ac.za; https://orcid.org/0000-0002-6565-2507

G.M. Bybee, P.A.M. Nex and B.A. Jogee
School of Geosciences, University of the Witwatersrand, 1 Jan Smuts Avenue, Braamfontein 2000, Johannesburg, South Africa
e-mail: Grant.Bybee@wits.ac.za; paul.nex@wits.ac.za; bibi.jogee1@wits.ac.za

Abstract

This paper assesses a poorly studied outcrop of orbicular granite from the Matopos granite batholith in the Diana's Pool area, Zimbabwe. Historical samples from Diana's Pool exhibit closely packed orbicules in a granitic matrix. They are 9 to 14 cm in diameter and are characterised by different types of orbicules containing coarse-grained felsic cores, fine-grained and alternating ferromagnesian and feldspathic shells, and a coarse-grained matrix. The orbicules are generally spherical to ellipsoidal in shape, however, some appear to be abraded and deformed. The compositions and grain sizes of cores and the matrix are comparable. Both the matrix and the cores are medium- to coarse-grained and dominated by plagioclase (the matrix probably in slightly lesser proportions), microcline (in variable proportions, and seemingly absent in some cores), quartz, biotite and accessory hornblende and magnetite. Contrary to the cores and matrix, shells are fine-grained and exhibit polygonal textures. In addition to this, the shells are dominated by biotite and magnetite; however, they do not contain hornblende. Plagioclase shows an almost complete overlap of An contents, $\bar{x} = 26 \pm 2.3$ (core), $\bar{x} = 24 \pm 0.9$ (shell) and $\bar{x} = 25 \pm 2.0$ (matrix). Biotite composition in the shells is significantly less magnesian ($\bar{x} = 16 \pm 2.4$) than in core ($\bar{x} = 27 \pm 2.2$) and matrix ($\bar{x} = 25 \pm 2.2$), whose compositions overlap. Average initial $^{87}Sr/^{86}Sr$ ratios from plagioclase in all the analysed shells ($\bar{x} = 0.70226$) are slightly more radiogenic than in the matrix ($\bar{x} = 0.70193$) and cores ($\bar{x} = 0.70187$). Cores are autoliths, which are plagioclase-rich, cumulate, or rim fragments reworked by new magma inputs or injections. Heterogeneous nucleation leading to the formation of orbicular shells around the cores is attributed to adiabatic decompression of magma pulses ascending in dykes, leading to superheating and resorption of early solids, and volatile exsolution, inducing undercooling, supersaturation, and shell crystallisation. The coarse-grained matrix crystallised later, after the orbicules formed, creating the groundmass and locking the orbicules in place. The deformation of shells and cores suggests that the orbicules continued to evolve in the presence of a melt (matrix material). As part of the Matopos Hills World Heritage Site, the Diana's Pool orbicular granites present a unique and noteworthy petrogenesis, which should be preserved as part of the region's important geoheritage.

Introduction

Since their discovery in the early 1800s, orbicular rocks have received attention because of their beauty and scarcity (von Buch, 1802; Leveson, 1963). To date, more than three hundred occurrences of orbicular rocks, from every continent have been described (Barbey, pers. comm., 2023), in different tectonic settings and hosted in lithologies of varying compositions (Sederholm, 1928; Ray, 1952; Leveson, 1966; Palmer et al., 1967; Garvie, 1969; Barrière et al., 1971; Garvie, 1971; Couturié, 1973; Enz et al., 1979; Vernon, 1985; Symes et al., 1987; Ort et al., 1992; Monod et al., 1995; Smillie and Turnbull, 2013; McCarthy et al., 2016; McCarthy and Müntener, 2016; Barbey et al., 2021; Zhang and Lee, 2021). In orbicular rocks, layers are concentrically arranged around central cores (Leveson, 1966; Zhang and Lee, 2021; Barbey et al., 2021) and this is atypical of igneous rocks, that exhibit layering, in which minerals are typically parallel (schlieren layering) or perpendicularly arranged (comb layering; Moore and Lockwood, 1973). Since the early 20th century, the authors mentioned above and others have carried out studies on orbicular bodies, establishing the following general characteristics:

- Orbicular bodies are usually small and rare, likely reflecting very specific conditions of formation. According to Leveson (1963) and Elliston (1984), orbicular textures are not dependent on a specific magma composition and the texture is more likely related to physical conditions during orbicular rock formation.
- Orbicular bodies frequently have an uneven shape and are small, measuring tens to hundreds of metres.
- They are frequently found on the margins of igneous intrusions.
- Shells with distinct mineral abundances and textures around a central core characterise the orbicular rocks.
- The orbicules (cores and shells) are always surrounded by a matrix.
- Orbicular rocks occur in both undersaturated and oversaturated ultramafic to silicic igneous or metamorphic rocks.
- The matrix can have variable compositions and textures (granitic, pegmatitic or dioritic).
- The host rock composition and mineral assemblages are typically distinguishable from the orbicules.
- The orbicules vary in shape, typically spheroidal to ellipsoidal. Orbicules that are more complex are also known, reflecting deformation (e.g., Ray, 1952; Lahti, 2005; Barbey et al., 2021).
- The central orbicular cores are generally igneous rocks that are granitic, dioritic and gabbroic in composition. The cores can also be single crystals or metamorphic fragments.
- Orbicular shells generally contain K-feldspar, plagioclase, quartz, amphibole, pyroxene and biotite, which are radially oriented.

The diversity of geological settings in which orbicular rocks occur and the variation in mineralogical, textural and chemical characteristics that they exhibit hinders a construction of a common petrogenetic hypothesis (Leveson, 1963; Leveson, 1973; Symes et al., 1987; Decitre et al., 2002). Although a magmatic origin is seldom questioned, no single mechanism is capable of explaining the formation of all types and features of orbicules. Instead, various models ranging between magmatic (e.g., Sederholm, 1928; Palmer et al., 1967; Vernon, 1985; Symes et al., 1987; Monod et al., 1995; Smillie and Turnbull, 2013; McCarthy and Müntener, 2016; Diaz-Alvarado et al., 2017; Barbey et al., 2021; Zhang and Lee, 2021; Li et al., 2021) and metamorphic (e.g., Leveson, 1963; Leveson, 1973; Moore and Lockwood,1973; Thompson and Giles, 1974) have been proposed to explain their genesis.

In recent years, and in addition to liquid immiscibility and devitrification models, two main magmatic models were proposed:

- a model of outward crystallisation from a core within dykes (McCarthy and Müntener, 2016; Barbey et al., 2021), but following to some extent previous researchers such as Vernon (1985) among others; and
- a model of magma interaction proposed by Zhang and Lee (2021), which considers slow quenching of hotter, more mafic magma globules incorporated into a cooler, more felsic magma.

The Diana's Pool orbicular granite body is located in the Matopos Hills of Zimbabwe. Garvie (1969; 1971) described it briefly but limited petrological and geochemical work appears to have been published. Previous work on the Diana's Pool orbicules lacks detailed mineral chemistry and isotope data to support conclusions about the genesis of these rocks. This paper is the first paper describing this southern African locality using modern technology including micro-XRF imagery and full thin section petrography, *in-situ* mineral compositions, and *in-situ* isotopic determinations, not only to gain a better understanding of the petrogenesis, but also to contribute to the geoheritage of this important site. As the locality is within the Matopos Hills World Heritage Site (Broderick and Hubbard, 2016), samples used in this study are from the historical collections housed in the Bleloch Museum collection of the School of Geosciences at the University of the Witwatersrand, South Africa.

Geological setting

The Diana's Pool orbicular granite body is exposed in the Matopos Hills area, 30 km south of Bulawayo, Zimbabwe (Figure 1; Garvie; 1969; 1971). This area is made up of the Matopos granite batholith, which is composed of the Matopos granite, a part of the 2.65 Ga Chilimanzi granite Suite (Garson, 1995; Smith and Fripp, 1973; Broderick and Hubbard, 2016). The Chilimanzi Suite intrudes the older Archean granite-greenstone terrane making up the Zimbabwean Craton (Garson, 1995). Available strontium isotope data from Hawkesworth and Bickle (1976) are consistent with an origin of the Chilimanzi Suite from melting of pre-existing silicic crust. The Matopos granite batholith (Figure 1) is an irregular oval body (~100 km east-west and ~30 km north-south) that is bounded in the north by the Bulawayo greenstone belt, the Gwanda and the Antelope greenstone belts in the south and the Filabusi greenstone belt in the east (Smith and Fripp, 1973).

The first scientific work done on the Matopos granite batholith was by Mennell (1902), who described the batholith as a microcline-biotite granite, remarking on its gneissic margin near Bulawayo and attributing this foliation to movement before consolidation. Amm (1940), who mapped the Bulawayo greenstone belt, described the Matopos granite batholith as intrusive to the basement schists and older gneissic granite. The Matopos granite has a northeasterly trending foliation and small mafic inclusions of amphibole-bearing material (Garvie, 1971). According to Smith and Fripp (1973), the Matopos granite comprises microcline (34%), oligoclase (33%), quartz (27%) and biotite (14%). The Matopos granite is granitic in composition, with K_2O/Na_2O values between 1.0 to 1.5, with an average K_2O/Na_2O ratio of 1.43, calculated from nine specimens collected within the batholith (Smith and Fripp, 1973).

Using Harpum's (1963) classification of granites based on alkali ratios, a study by Smith and Fripp (1973) shows that the Matopos granite porphyry is highly heterogeneous and all the chemical analyses available to date show a wide compositional variation of the Matopos granite. The studied Diana's Pool orbicular granite body (Figure 1b) occurs as a small body within the Matopos granite (Smith and Fripp, 1973). According to Garson (1995), mineralogical, structural and chemical evidence indicates that the interaction of Matopos granite and the greenstone belt material produced a contact facies zone of rocks, which are regarded as "older granites". Gradual and intimate spatial associations characterise these contact facies and the orbicular granite body is associated with them and outcrops at the Diana's Pool area (Smith and Fripp, 1973; Garvie, 1997; Garson, 1995). According to Garson (1995), the interstitial material that makes up the cores and the matrix between the orbicules is similar in composition to the host Matopos granite; however, biotite is more abundant. An approximately 13 m wide, northwest-trending dolerite dyke to the west, an intrusion of a coarse-grained Mbalabala granite porphyry, and the Matopos granite are the only other rock types near the orbicular granite locality (Figure 1; Garson, 1995).

Sampling and analytical methods

In the past century, samples from Diana's Pool (BM14780a, b, and c) were curated at the Bleloch Museum in the School of Geosciences at the University of the Witwatersrand. The School granted permission for the use of these samples in this study. Hand sample BM14780B was sent to MinTek in Johannesburg, South Africa, for micro-XRF analyses to generate element maps to investigate the elemental distribution within the samples and enable the identification of particular phases and areas of interest by providing supplementary information at a larger scale of observation. A voltage of 50 kV, anode current of 599 µA, spot size of 20 µm and a chamber pressure of 2 mbar were used during the sample analysis. Five thin sections were made from hand samples, and they were used for detailed petrographic analyses. Sample BM14780A is representative of the matrix, BM14780D represents the core, BM14780F represents the full orbicule (core, shell and matrix), and BM14780G and BM14780E represent shells. The thin sections were scanned at high resolution using an Olympus BX 63 optical microscope at the University of the Witwatersrand ahead of detailed textural analyses using a TESCAN Integrated Mineral Analyser (TIMA). Phase and element maps of the samples were obtained by energy-dispersive X-ray spectroscopy (EDS) using the VEGA3 SEM instrument and the VEGA 3 TESCAN TIMA 1.7.0 software. The beam parameters were 25 kV accelerating voltage, 43 µA emission current, working distance of 15 mm, specimen beam current of 17.68 µA, absorption current of <1 pA, gun pressure of 1.63 x 10^{-3} Pa, and a spot size of 590 nm. Mineral chemical analyses were performed on the samples using a CAMECA

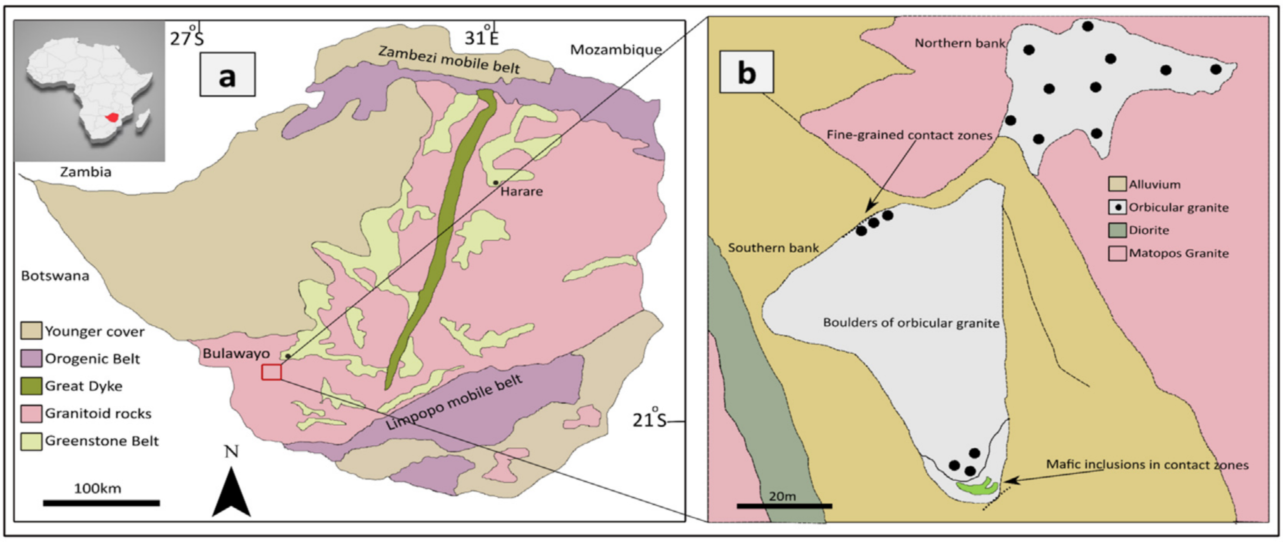

Figure 1. *Geological map of the Matopos Hills and Diana's Pool area: **(a)** Geological map of the Matopos granite and the surrounding rock types, modified after Broderick and Hubbard (2016). The red square shows the study area (Diana's Pool). **(b)** Simplified geological sketch map of the orbicular granite outcropping 400 m downstream of Diana's Pool, modified after Garson (1995).*

SX-5-FE electron probe at the University of the Witwatersrand. An acceleration voltage of 15 keV and beam current of 20 nA were used for analysing the minerals. These analytical measurements were accompanied by standards for each analysis type, which produced acceptable values. Recorded counting times were ten seconds on peak and five seconds on the background. The data were collected using CAMECA software and an automated XPHI matrix algorithm was used for matrix effect correction. Mineral formulas were calculated on the basis of stoichiometry and charge balance. The complete major element chemistry data is included in Supplementary Data Table 1 and 2 for plagioclase and biotite, respectively. (Supplementary data files are archived in the South African Journal of Geology repository (https://doi.org/10.25131/sajg.127.0021.sup-mat)).

In-situ $^{87}Sr/^{86}Sr$ isotope analyses were conducted using a laser ablation system connected to a Nu Plasma II multicollector (MC)-ICP-MS system at the University of Johannesburg, South Africa. $^{87}Sr/^{86}Sr$ ratios in plagioclase were measured on representative thin sections using a spot ablation method and a spot size of 100 µm for 60 seconds. Laser energy was set at 6 mJ with a frequency of 10 Hz and an attenuator value of 50%, resulting in an on-sample fluence of approximately 3.5 J cm^2. Detector set-up was as follow: H5 = ^{88}Sr (+ $^{176}Yb^{2+}$); H3 = ^{87}Sr + ^{87}Rb (+ $^{174}Yb^{2+}$); H1 = ^{86}Sr (+ $^{172}Yb^{2+}$); L1 = ^{85}Rb (+ $^{170}Er^{2+}$ + $^{170}Yb^{2+}$); L3 = ^{84}Sr + ^{84}Kr (+ $^{168}Er^{2+}$ + $^{168}Yb^{2+}$) and IC1 = ^{82}Kr (+ $^{164}Er^{2+}$). The background was subtracted from the ablation signal. Krypton was monitored on mass 83, but no corrections were necessary. The Nu Plasma NICE data processing program was used to do background subtraction and all other computations. This tool also estimates 1SE for reported values, taking into account the individual points and the integration period. The accepted $^{86}Sr/^{88}Sr$ ratio of 0.1194 was used in the calculations for the Sr mass bias adjustment. The ^{87}Rb contribution was calculated from the ^{85}Rb signal using the standard $^{87}Rb/^{85}Rb$ ratio of 0.3858. The secondary standards used to evaluate accuracy were the Rb-free in-house plagioclase glass standard ($^{87}Sr/^{86}Sr$ = 0.70719 ± 2 (2SD on 3 TIMS determinations: Elburg, unpublished; Maghdou-Mashhour, 2021); reference glass BHVO2G ($^{87}Sr/^{86}Sr$ = 0.703469 ± 0.000014; Elburg et al., 2005) and a calcite reference material WC-1 (Roberts et al., 2017; Rasbury et al., 2021). These standards were measured every 5 to 10 unknowns. Reference materials reproduced the aforementioned accepted values for BHVO2 with $^{87}Sr/^{86}Sr$ 0.703386 ± 0.000083 (n = 3), the in-house plagioclase standard produced an average $^{87}Sr/^{86}Sr$ of 0.707104 ± 0.000045 (n = 2) and the WC-1 standard produced an average $^{87}Sr/^{86}Sr$ of 0.706817 ± 0.000015 (n = 7). Our plagioclase $^{87}Sr/^{86}Sr$ data are included in Supplementary Data Table 3. Some analyses have Rb/Sr ratios that are too high for plagioclase, implying that there was alteration and the calculated initial $^{87}Sr/^{86}Sr$ values are not representative of the igneous value.

Results

Hand sample descriptions

The orbicular samples are characterised by a granitic inter-orbicular matrix (30% rock volume) with closely packed orbicules (70%; Figure 2a, b and c). The orbicules are generally spherical to ellipsoidal in shape, however, some orbicules appear to have been abraded, where the cores seem to be intact but large parts of the shells have been removed (Figure 2c). Some orbicules have been deformed where layers in the shells are bent (black arrow, Figure 3a), possibly resulting from indentation on interaction with other orbicules. Shells that incorporate and surround matrix material, which has moved into one segment of the shell, creating a thickening or pocket (blue arrow, Figure 2e), characterise some of the Diana's Pool orbicules. The orbicules range in size from 5 to 14 cm in diameter (Figure 2a). Different types of orbicules characterise the hand samples: orbicules characterised by felsic cores with dark ferromagnesian shells (Figure 2a); orbicules characterised by felsic cores with dark and felsic shells (Figure 2b); more complex orbicules characterised by cores with abundant coarse-grained hornblende and biotite (Figure 2e).

Micro-XRF imagery and petrographic descriptions

Prior to thorough petrographic descriptions, element maps illustrating the distribution of elements in the orbicular cores, shells and the matrix were produced using a qualitative micro-XRF scan of sample BM14780B (Figure 3).

Cores

Medium- to coarse-grained (2 to 5 mm) cores consist of plagioclase (60%) and K-feldspar (10%; the latter in variable proportions, and seemingly almost absent in some cores), plus quartz (10%) and ferromagnesian phases (20%; Figures 3a; 4 and 5).

Approximately 75% of the plagioclase in the cores is sericitised (Figure 4a) and unaltered plagioclase occurs as subhedral to euhedral (0.1 to 6 mm) grains. Quartz is minor (<10%), with modal variations from one core to another as shown by variations in Si (Figure 3a and b).

The predominant K-feldspar in the cores is microcline (5%; Figures 4 and 5), which occurs as an interstitial phase (Figure 6d). Myrmekite textures are common between quartz and plagioclase (Figure 6c). The highest contents of Fe are observed where there are irregular and locally concentrated patches of ferromagnesian minerals (Figure 3a and c). Biotite (3%) and hornblende (2%; Figures 4a, b and 6b) are the dominant ferromagnesian mineral assemblages in cores and they are often irregular in shape. Hornblende, as indicated by high Fe (Figure 3a and c) and Ca (Figure 3a and e) content is variable and the mineral is not present in all orbicular cores (Figure 3a).

Shells

Sharp contacts mark the boundaries between cores and shells (Figures 2a, b; 3; 4; 5 and 6a). From cores to the inner shells, the modal abundance of felsic minerals, grain size, and plagioclase alteration all decrease (Figures 3; 4; 5 and 6a). Alternating fine-grained ferromagnesian (as shown by high Fe contents; Figure 3a and c) and feldspathic layers (as shown by high Ca and K contents; Figure 3a, d and e) characterise the

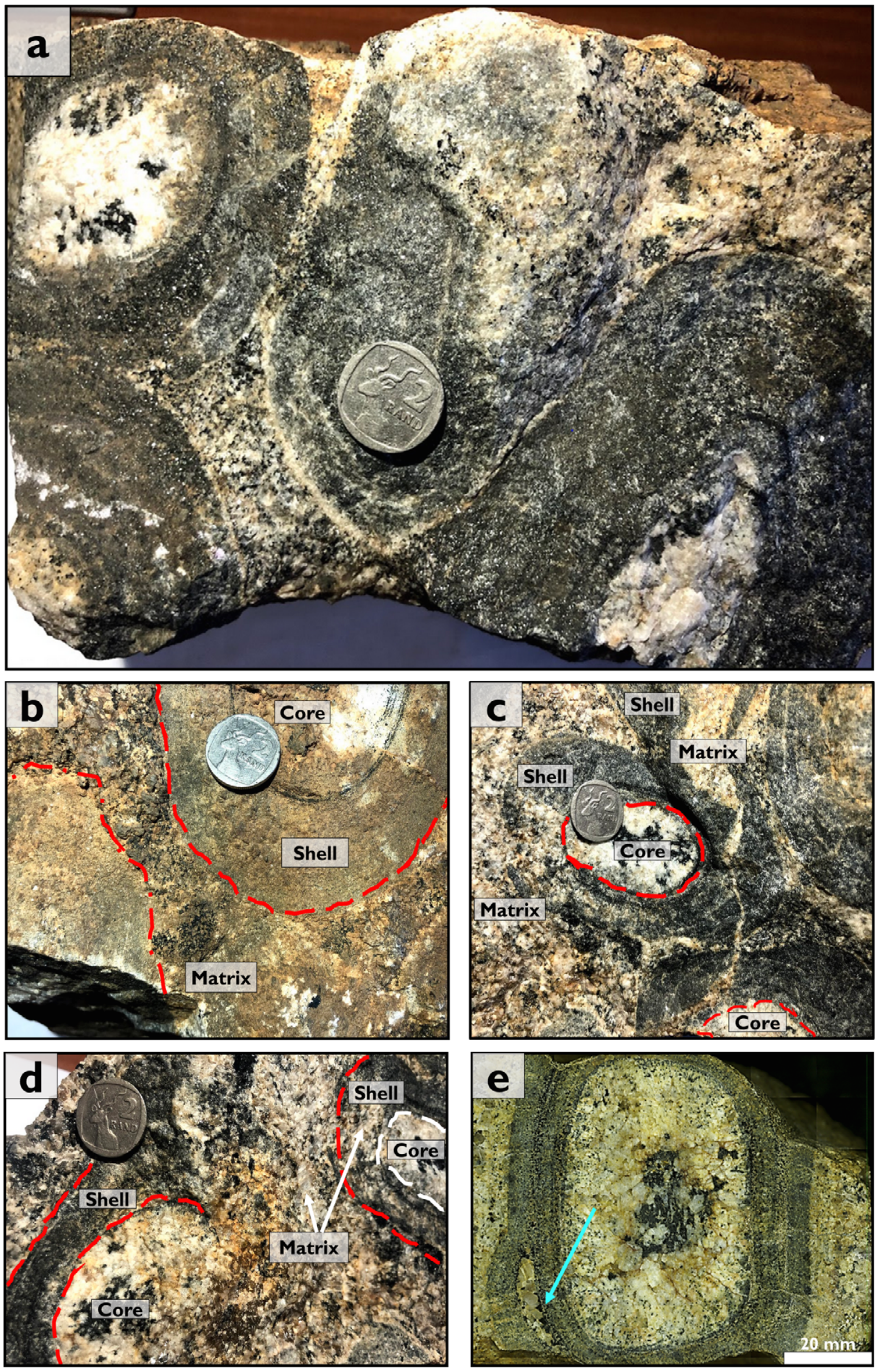

Figure 2. *Orbicular granite samples from the Diana's Pool area: **(a)** A sample showing the general appearance of Diana's Pool orbicules. These spherical to ellipsoidal and triaxial orbicules make up approximately 70% of the rock volume and are characterised by felsic and medium-grained cores that are dominated by feldspars and patches of dark hornblende surrounded by alternating mafic and felsic shells in a granitic host matrix. **(b)** Closely packed orbicules surrounded by a coarse-grained matrix. The red dotted lines show the sharp contacts between orbicules and the host matrix. **(c)** and **(d)** Matrix cross cutting the mafic orbicular shells and the felsic cores. **(e)** Inclusions of the granitic host matrix material (blue arrow) in mafic shells creating a "saddle reef". The coin is 23 mm in diameter.*

Diana's Pool orbicular shells. The mafic shells are dominated by biotite (40%) and magnetite (30%) with minor plagioclase (20%) and quartz (10%). Conversely, plagioclase (45%), quartz (15%) and minor biotite (10%) and magnetite (20%) dominate the felsic shells (Figures 4 and 5). Plagioclase throughout layers of the shells show little change in grain-size, forming a mosaic of crystals characterised locally by polygonal textures (red arrow; Figure 6e and f).

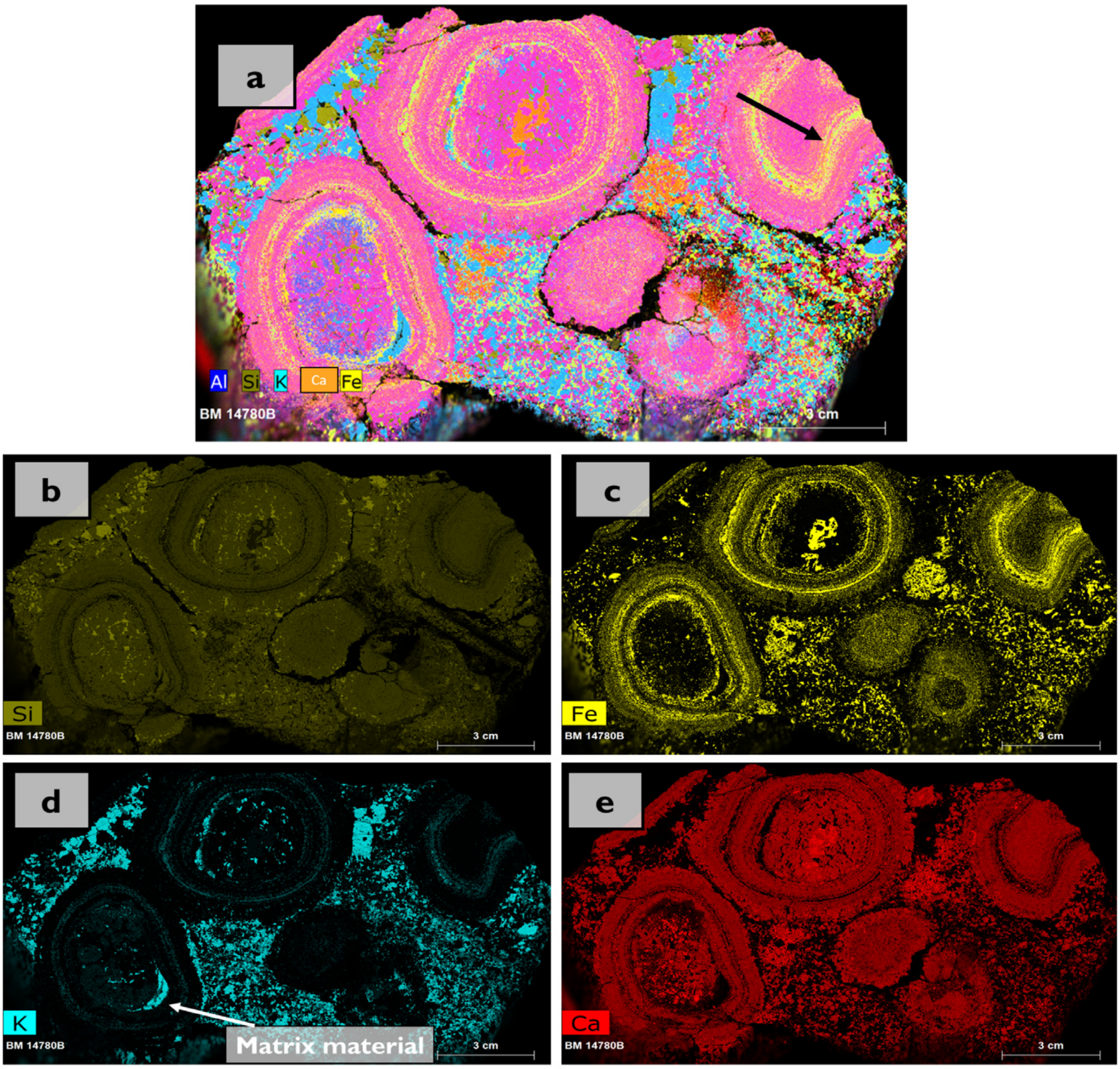

Figure 3. *Micro-XRF element maps of orbicular sample BM 14780B: **(a)** A composite of selected element showing elements detected via the normal map spectrum. Magenta is a combination of Si and Ca. **(b)** Element map showing uniform distribution of Si in cores and the matrix however, high intensities of Si are observed in the matrix. **(c)** Element map showing high distribution and intensities of Fe in shells, matrix and some parts of the cores. **(d)** Element map showing the highest concentrations and intensities of K in the matrix, the granitic matrix between the shells, and some parts of the cores. **(e)** Element map showing the distribution and concentrations of Ca in different parts of the orbicules.*

The degree of sericitisation of plagioclase in shells is notably lower than in the cores. It is also important to observe the increase in Fe (Figure 3a and c) concentrations from cores to the concentric shells, indicating the presence of biotite and magnetite (Figures 4; 5 and 6f). The radially-oriented magnetite (20%) and biotite occur as intergranular masses between feldspar and form a radiating texture or comb-layering (yellow arrows; Figures 4 and 5b) that is restricted to the shells. Some of the shells (e.g., outer shell, Figure 5b) are formed by biotite (>80%) and minor plagioclase, and some mostly by magnetite and minor plagioclase (e.g., inner shell and Figure 5b). Contrary to cores and matrix, neither feldspathic nor ferromagnesian shells contain hornblende, but only biotite, magnetite and plagioclase (Figures 4 and 5).

Matrix

Sharp contacts mark the boundaries between outer shells and the matrix (Figures 2b; 3; 4; 5 and 6f). The matrix is granitic and coarse-grained (6 to 7 mm; Figures 2b; 5b, d and 6f). An increase in grain size (Figure 6), as well as an increase in feldspar (indicated by high Ca, K and Al contents; Figure 3a, c, d and e) and quartz (as shown by high Si contents and Figure 3b), and a decrease in magnetite modal abundances

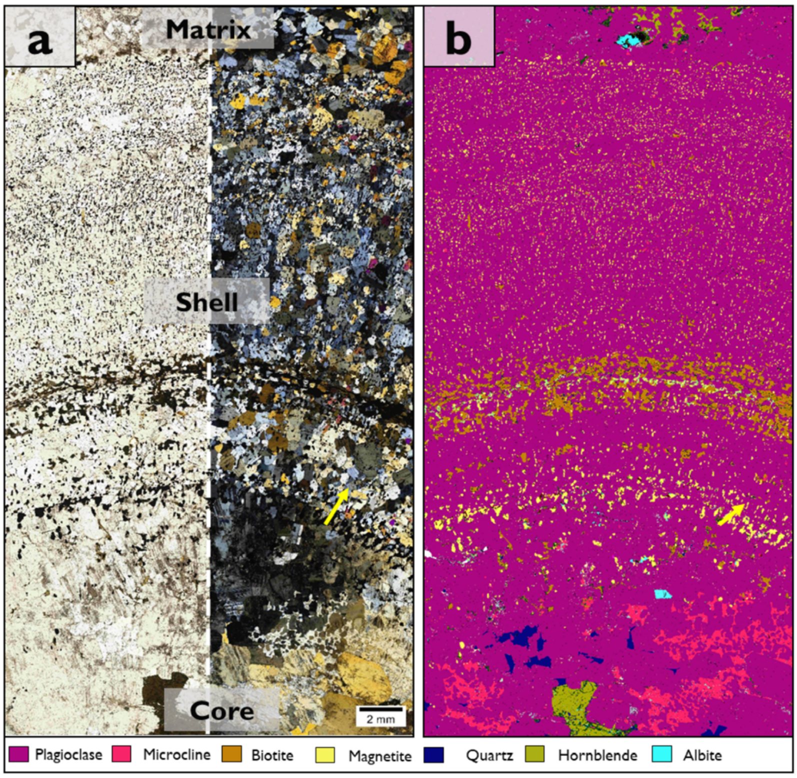

Figure 4. *Full thin section photomicrographs of orbicular samples: (**a**) Full thin section images of sample BM14780F in plane-polarised (left) and under cross-polarised light (right). (**b**) TESCAN Integrated Mineral Analyser (TIMA) image of the Diana's Pool orbicular sample BM14780F showing medium-grained cores dominated by feldspars, quartz and hornblende; fine-grained and alternating mafic and felsic shells dominated by feldspars, biotite and magnetite and the coarse-grained matrix dominated by feldspars and hornblende.*

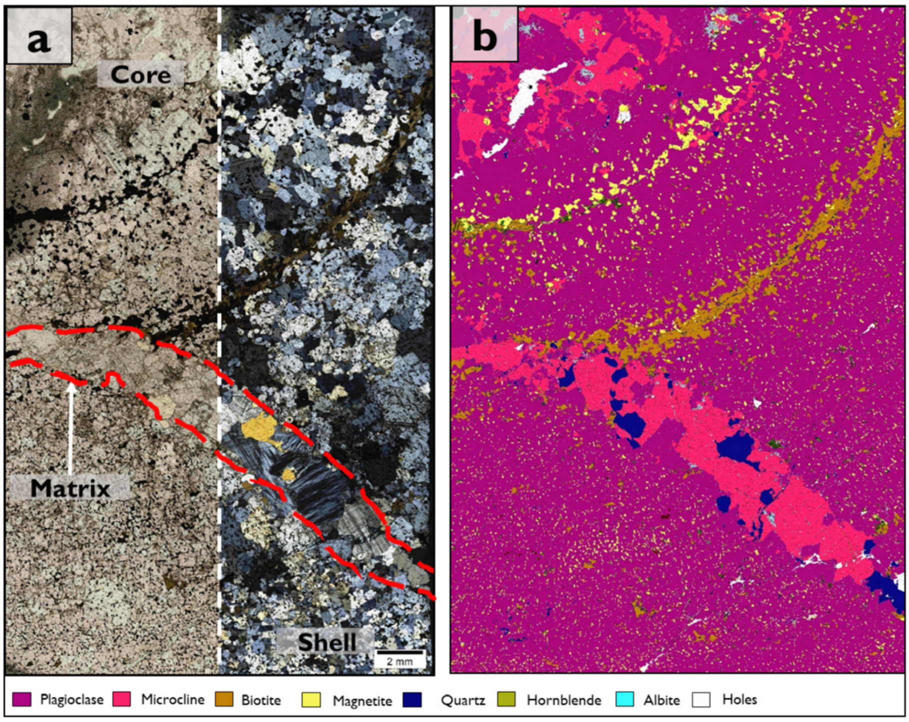

Figure 5. *Full thin section photomicrographs of orbicular samples: (**a**) Full thin section images of sample BM14780H in plane-polarised (left) and under cross-polarised light (right). (**b**) TESCAN Integrated Mineral Analyser (TIMA) image of the Diana's Pool orbicular sample BM14780H showing fine-grained cores crosscut by a coarse-grained granitic matrix.*

(as shown by high Fe contents and Figure 3c) also mark the transition from outer shells to the matrix. The matrix composition and grain-size are comparable to that of cores (Figures 4 and 5). The matrix comprises plagioclase (30%), microcline (30%), orthoclase (4%), quartz (25%), biotite (3%), chlorite (3%), and accessory hornblende and magnetite (Figures 4; 5 and 6g). The modal abundances of microcline (high K contents; Figure 3a and d) and quartz are higher in the matrix (high Si contents; Figure 3a and b) than in cores and shells. Quartz occurs as granophyric intergrowths with microcline in places (Figure 6h). Locally, hornblende occurs as an interstitial phase enveloping touching grains of feldspars and quartz (Figures 4a, b and 6g). Some of the samples are characterised by shells that are crosscut by veins of the felsic matrix (Figures 2c, d; 5a and b) and the contact where the matrix intrudes the shells is sharp (Figure 5).

In summary, the compositions and grain sizes of cores and the matrix are comparable, both the matrix and the cores are medium- to coarse-grained and dominated by plagioclase (the former probably in slightly lesser proportions), microcline (in variable proportions, and seemingly absent in some cores), quartz, biotite and accessory hornblende and magnetite. Contrary to cores and matrix, shells are fine-grained and exhibit polygonal textures. In addition to this, shells are dominated by biotite, magnetite and plagioclase; however, they do not contain hornblende.

In-situ compositions of mineral phases

In order to understand the evolution of the magma(s) and the processes that were taking place during crystallisation, major element compositions of plagioclase and biotite, as well as in-situ $^{87}Sr/^{86}Sr$ compositions, were determined in the orbicular cores, shells, and matrix of Diana's Pool orbicules. Table 1 lists the analysed samples along with the minerals in each sample's respective orbicular structure.

Plagioclase

Major elements in cores, shells, and matrices of several orbicule samples were analysed in unaltered plagioclase grains (Table 2). The ranges of SiO_2, CaO, K_2O, Al_2O_3 and Na_2O in (wt. %) in cores, shells and matrices of different samples are shown in Table 2 and the rest of the elemental data are presented in the Supplementary Data Table 1.

The data were plotted on the variation diagrams (Supplementary Data Figure 1), which show the variation of selected elements (apfu) between plagioclase from different orbicular samples plotted against Si (apfu). Owing to data dispersion, there is no interpretable differences in Na (Supplementary Data Figure 1c) and K (Supplementary Data Figure 1d) between the samples. Samples BM14780F and BM1478080G form a specific cluster (core, shell and matrix) with Si around 2.6 apfu (Supplementary Data Figure 1), rather high alumina (between 1.4 and 1.5 apfu; Supplementary Data Figure 1a) and low Ca (~0.3 apfu; Supplementary Data Figure 1b). Samples BM1478080E and 80D have higher Si (around 2.6 and 2.8 apfu; Supplementary Data Figure 1) and low Al (1.1 to 1.3 apfu; Supplementary Data, Figure 1a). There are two groups of matrix plagioclase, one with low Si (between 2.5 and 2.6 apfu) and high Al (between 1.4 and 1.5 apfu; Supplementary Data Figure 1a), and the other with high Si (between 2.6 and 2.9 apfu and low Al (between 1.1 and 1.3 apfu; Supplementary Data Figure 1a) close to compositions of samples BM1478080E and BM1478080D.

Plagioclase crystals are sodic and regardless of textural position (cores, shells or matrices) plot mainly in the oligoclase field on the feldspar ternary classification diagram, with a few grains bordering on the andesine field (Figure 7a).

Samples BM14780F (An_{23-27}) and BM14780G (An_{24-25}) contain shells composed of plagioclase that is more sodic than the more calcic plagioclase in shells from sample BM14789E (An_{24-31}).

Table 1. Table showing different samples that were analysed for EPMA and *in-situ* $^{87}Sr/^{86}Sr$. Bt=biotite and Pl=plagioclase.

Sample	BM14780A	BM14780D	BM14780E	BM14780F	BM14780G
Core		Pl, Bt & $^{87}Sr/^{86}Sr$		Pl, Bt & $^{87}Sr/^{86}Sr$	
Shells			Pl, Bt & $^{87}Sr/^{86}Sr$	Pl, Bt & $^{87}Sr/^{86}Sr$	Pl & Bt
Matrix	Pl, Bt & $^{87}Sr/^{86}Sr$			Pl & Bt	

Table 2. Table showing the ranges of major elements (wt.%) in plagioclase from cores, shells and matrices of differed Diana's Pool orbicular samples.

Structure	Cores		Shells			Matrices	
Sample#	BM14780D	BM14780F	BM14780E	BM14780G	BM14780F	BM14780F	BM14780A
SiO_2	59.5-61.2	56.8-58.1	60.1-61.7	57.3-58.1	57.0-58.0	56.4-59.1	53.8-64.1
Al_2O_3	24.1-24.7	26.8-27.8	22.7-24.3	26.5-27.5	36.3-27.3	26.5-28.0	21.1-29.2
CaO	5.0-5.8	4.9-5.7	5.7-6.0	5.2-5.4	5.0-5.5	4.6-6.0	2.8-7.5
Na_2O	8.7-9.4	7.4-9.1	6.7-9.4	8.5-8.9	8.1-9.3	7.7-9.1	7.6-10.0
K_2O	0.1-0.2	0.1-0.4	0.2-0.4	0.5-0.4	0.1-0.3	0.1-1.2	0.1-0.5

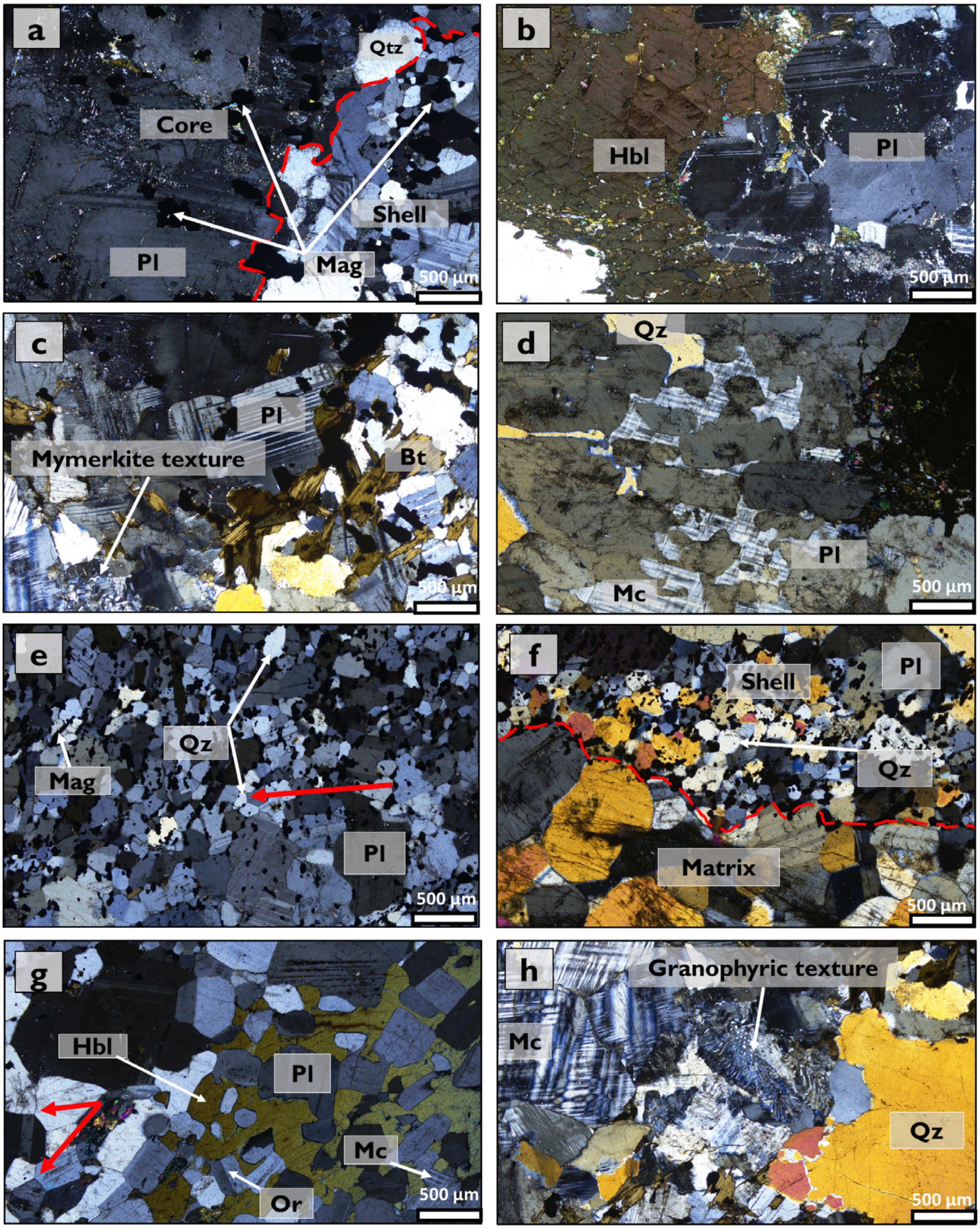

Figure 6. *Photomicrographs of representative features of Diana's Pool orbicules: **(a)** Sharp contact (red-dotted line) between the coarse-grained core and the fine-grained shell. Feldspars and minor magnetite dominate the core. Equigranular grains of feldspars and quartz dominate the shells, and there is a notable increase in magnetite concentration in the shell. **(b)** Large and irregular grains of hornblende adjacent to feldspars in the cores. **(c)** Quartz and plagioclase overgrowth forming myrmekite textures. **(d)** Interstitial quartz and microcline enveloping larger plagioclase grains. **(e)** Fine-grained shell dominated by plagioclase, magnetite, biotite and quartz. Plagioclase shows little change in grain-size throughout the shells, occurring as a mosaic of granular crystals that form polygonal textures. Magnetite form radiating textures in shells. **(f)** Sharp contact between a fine-grained shell and a granitic matrix. **(g)** Interstitial hornblende enveloping euhedral and touching grains of plagioclase (red arrow showing plagioclase) in the matrix. **(h)** Quartz and K-feldspar overgrowth forming granophyric textures in the matrix.*

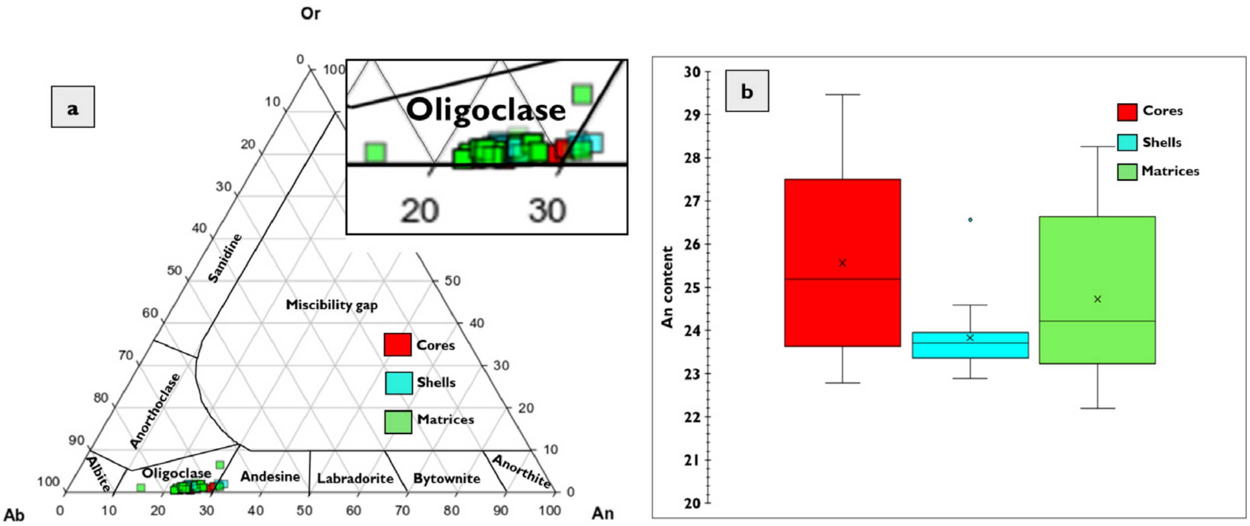

Figure 7. *Diagrams of plagioclase chemical composition: **(a)** A classification of feldspars from Diana's Pool orbicules on a ternary albite-anorthite-orthoclase diagram. **(b)** The graph showing An content in plagioclase from Diana's Pool orbicular cores, shells and matrices from the representative sample BM14780F. The graph shows ranges that are more restricted in An contents in cores (26 ± 2.3), shells (24 ± 0.9) and the matrix (25 ± 2.0).*

Sample BM14780F ($An_{23\text{-}29}$) cores contain plagioclase that is more calcic than in cores from sample BM14780D ($An_{22\text{-}26}$). Sample BM14780F matrix ($An_{22\text{-}28}$) contains plagioclase that is slightly more sodic than in matrix from sample BM14780A ($An_{22\text{-}30}$). In summary, there is little variation in plagioclase composition observed in cores, shells and matrices from different orbicular samples. In sample BM14780F, which shows a full orbicule, plagioclase shows an almost complete overlap of An contents (Figure 7b) in core, shell, and matrix: $\bar{x}$ = 26 ± 2 (core), $\bar{x}$ = 24 ± 1 (shell) and $\bar{x}$ = 25 ± 2 (matrix). The An content in the inner ($\bar{x}$ = An_{24}) to middle ($\bar{x}$ = An_{24}) to outer ($\bar{x}$ = An_{24}) shells is homogeneous and shows little to no variation.

Biotite

Chemical compositions of biotite in cores, shells, and matrices were analysed. The analysed samples include samples BM14780F, BM14780G, BM14780A, and BM14780D (Table 1). The ranges between the major elements MgO, Al_2O_3, SiO_2 and TiO_2 are shown in Table 3 and the remainder of the elements are shown in the Supplementary Data Table 2.

Table 3. Table showing the ranges of major elements (wt.%) in biotite from cores, shells and matrices of differed Diana's Pool orbicular samples.

Structure	Core	Shells		Matrix
Sample#	BM14780D	BM14780G	BM14780F	BM14780A
SiO_2	36.8-43.9	37.0-38.7	36.0-42.9	36.5-44.0
TiO	2.1-2.8	2.0-4.0	1.6-3.7	1.8-4.0
Al_2O_3	13.6-18.0	14.8-15.8	14.9-16.2	12.9-18.3
MgO	4.4-5.7	2.7-3.6	1.8-3.9	4.1-5.9
FeO	21.5-25.0	24.9-27.3	23.7-27.2	22.4-32.2

Only a small number of samples were analysed since, unlike plagioclase, unaltered biotite is scarce in these samples. Moreover, due to substantial alteration only five analyses could be conducted. This alteration is reflected in K + Na values which are below two (Supplementary Data Table 2). It is crucial to note that these are the only available data points, given the highly altered nature of the core samples. Biotite analysed in the shell samples BM14780F and BM15780G show great compositional similarities (Table 3 and Figure 8). Both samples contain biotite characterised by homogeneous Al (between 1.4 and 2.3 apfu and Figure 8a) and Fe (between ~3.0 and 3.6 apfu; Table 3 and Figure 8b) contents. These shell samples are also characterised by a significant dispersion of Ti (Table 3 and Figure 8d) and lower Si compared to biotite from the matrix sample BM14780A and the core sample BM1480D (Table 3 and Figure 8c).

In general, shells comprise biotite that is less magnesian than biotite from the matrix and core samples (Figure 8, Supplementary Data Figure 3). However, there is a variation in Mg in biotite from different shell samples. Biotite from shell sample BM14780F is less magnesian than biotite from shell sample BM14780G (Figure 8).

The matrix sample BM14780A and the core sample BM14780A contain biotite with overlapping Mg contents (Figure 8). Using the MgO-FeO-Al_2O_3 ternary diagram after Abdel-Rahman (1994) and Nachit et al. (2005), biotite in Diana's Pool orbicular core, shells, and matrix plot in the peraluminous (S-type) granite suite (Supplementary Data Figure 2d) and they are all considered primary magmatic compositions, although some analyses fall outside the primary biotite field (Supplementary Data Figure 2c).

Following the nomenclature after Makutu et al. (2004) and Deer et al. (1992), biotite from the Diana's Pool cores, shells and matrices all plot in the annite field (Supplementary Data Figure 2a and b).

Biotite shows a systematic variation in Mg# from cores to shells to the matrix. Biotite composition in shells is significantly less magnesian ($\bar{x}$ = 16 ± 2) than in core ($\bar{x}$ = 27 ± 2) and

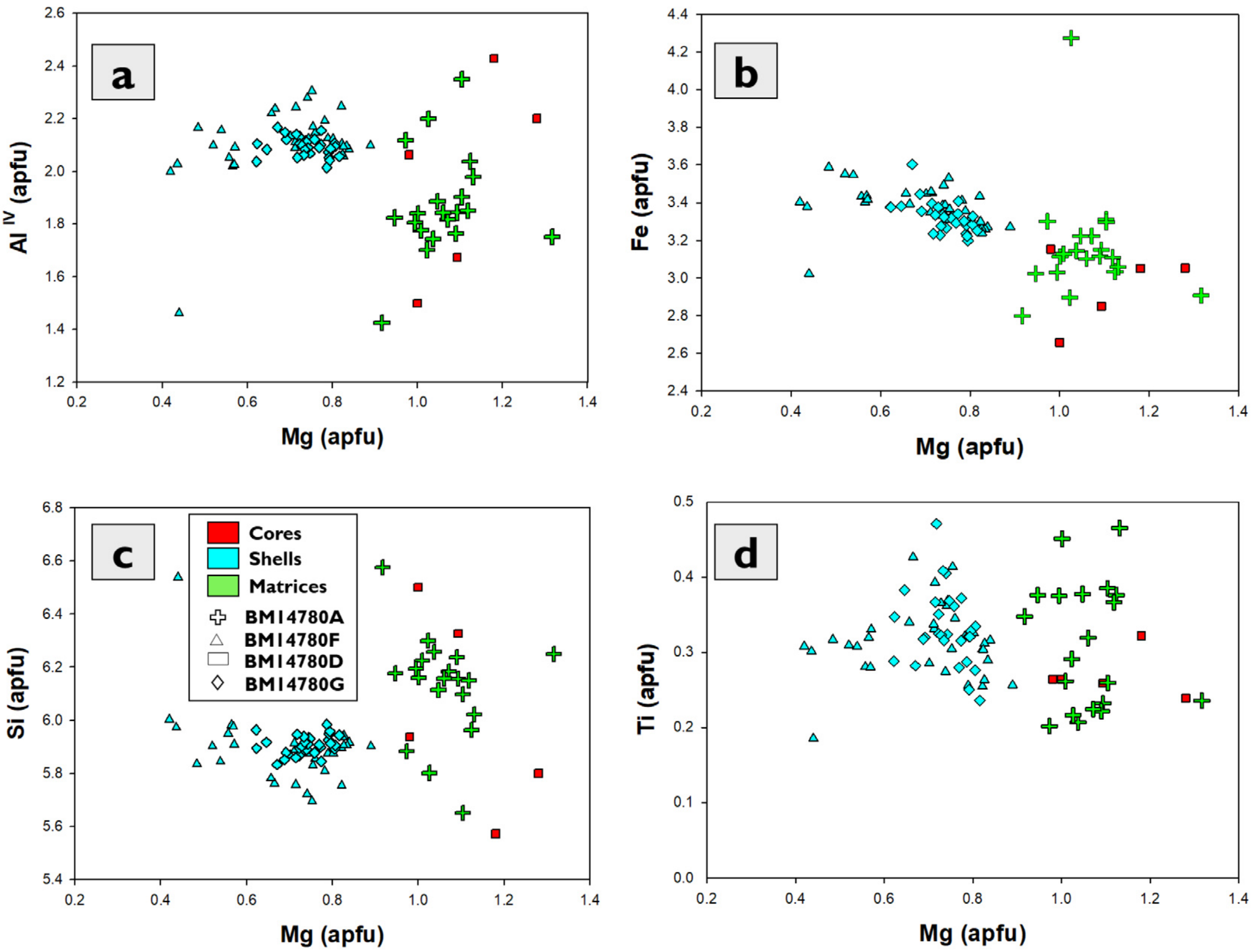

Figure 8. *Chemical variation diagrams showing variation of different elements in biotite from the Diana's Pool orbicular cores, shells and matrices plotted against Mg (apfu).*

matrix ($\bar{x}$ = 25 ± 2), whose compositions are overlapping (Supplementary Data Figure 3). Compared to the variation in plagioclase compositions, biotite seems to be homogeneous in shells of different samples, showing little variation in Mg#. The average Mg#s are 17 and 18 in samples BM14780F and BM14780G, respectively.

$^{87}Sr/^{86}Sr$ isotopes ratios in plagioclase

From the cores, shells, and matrices of several Diana's Pool samples, initial $^{87}Sr/^{86}Sr$ isotope compositions in plagioclase were determined to track and test the geochemical processes that led to the formation of these orbicular rocks (e.g., assimilation). The data ranges are presented in Table 4 and the rest of the isotopic data are presented in the Supplementary Data Table 3. The initial $^{87}Sr/^{86}Sr$ ratios (Table 4) were calculated using the estimated age of the Matopos granite of 2 650 Ma (Broderick and Hubbard, 2016). Plagioclase in the cores and the shells samples have slightly more radiogenic initial $^{87}Sr/^{86}Sr$ ratios than the less radiogenic ratios in plagioclase in the matrix (Table 4).

The initial $^{87}Sr/^{86}Sr$ ratios in cores, shells, and matrices generally show little variation (Table 4 and Figure 9) and most of the Diana's Pool orbicules comprise plagioclase that exhibit less radiogenic $^{87}Sr/^{86}Sr$ isotopic compositions than reference glass

Table 4. Table showing the ranges of initial $^{87}Sr/^{86}Sr$ in plagioclase from cores, shells and matrices of different Diana's Pool.

Structure	**Cores**		**Shells**		**Matrix**
Sample#	**BM14780D**	**BM14780F**	**BM14780E**	**BM14780F**	**BM14780A**
Initial $^{87}Sr/^{86}Sr$	0.700477 ± 0.000198 to 0.702407 ± 0.000163	0.701229 ± 0.000163 to 0.705350 ± 0.000169	0.701547 ± 0.000184 to 0.702758 ± 0.000182	0.701642 ± 0.000013 to 0.703423 ± 0.000171	0.700701 ± 0.000231 to 0.703188 ± 0.000274

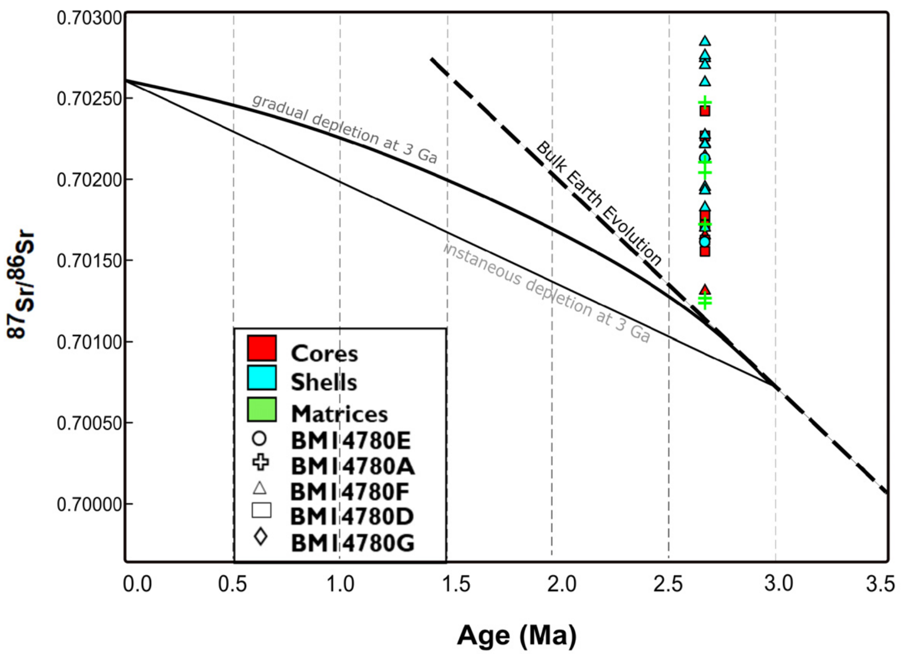

Figure 9. *Graph showing the initial $^{87}Sr/^{86}Sr$ ratios in the Diana's Pool orbicular cores, shells and matrix relative to Bulk Silicate Earth (Allègre et al., 1988; Workman and Hart, 2005; Bouvier et al., 2008) and Depleted Mantle (DePaolo and Wasserburg, 1976). Considering data scatter and analytical uncertainties there is no significant difference in $^{87}Sr/^{86}Sr$ between core samples BM14780F and BM14780D. There is some overlap of $^{87}Sr/^{86}Sr$ data between shell samples BM14780E and BM14780F, although plagioclase from shell sample BM14780F is slightly more radiogenic.*

BHVO2G ($^{87}Sr/^{86}Sr$ <0.703469 ± 0.000014 and Figure 9), although some analyses exhibit compositions that are more radiogenic (>0.703; Supplementary Data Table 3). These are too high for plagioclase, implying that there was alteration and the calculated initial $^{87}Sr/^{86}Sr$ values are not representative of the igneous value and are not shown in Figure 9. Considering data scatter and analytical uncertainties, there is no significant difference in $^{87}Sr/^{86}Sr$ between plagioclase from core samples BM14780F and BM14780D (Table 4). There is some overlap of $^{87}Sr/^{86}Sr$ data between shell samples BM14780E and BM1478080F, although shell sample 80F is more radiogenic (Table 4 and Figure 9).

Discussion

Comparing Diana's Pool orbicules with global orbicular granite occurrences

Diana's Pool orbicules show similar features to other orbicular localities described elsewhere and these features include:

- location at the margin of the intrusive body;
- presence of cores, shells, and an inter-orbicular matrix;
- shells of diverse mineral assemblages surrounding inner cores and;
- shells with radial textures.

However, similar to other orbicular localities, the origin of these orbicules remains poorly understood. The spatial relationships between the orbicular body and the host Matopos granite porphyry are not well characterised. However, it is reasonable to conclude that the orbicules formed from the Matopos granite magma that started crystallising prior to the formation of orbicules based on descriptions of the host Matopos granite and its resemblance to the orbicular matrix (Garson, 1995). Although we did not carry out any fieldwork and we lack an understanding of the appearance and arrangement of the orbicular body, the appearance of orbicular samples (large, small and fragmented orbicules crosscut by granitic veins; Figure 2c, d and e) suggest that the present form of the orbicular body is the result of sequential emplacement process involving different magma sources and magma injections containing orbicules (e.g., Barbey et al., 2021). Based on the deformation features (Figure 2c, d and e), it is plausible to suggest that the orbicules formed in deeper areas of the crust and were later emplaced in their present setting. They were most likely dragged by the inter-orbicular magma during a repeated sequential process.

Petrogenesis

Core formation

There is usually a central core in orbicular rocks, which can be a megacryst (e.g., Decitre et al., 2002), early crystallised material from the magma (e.g., Lindh and Näsström, 2006), an autolith (e.g., Barbey et al., 2021), or a xenolith (e.g., Elliston, 1984). Diana's Pool orbicular cores comprise subhedral to euhedral plagioclase grains that form aggregates and exhibit An contents that show an almost complete overlap with An of plagioclase in shells and the granitic matrix. This implies that they are most likely autoliths, which are plagioclase-rich cumulates, or rim fragments reworked by new magma inputs or injections (McCarthy and Müntener, 2016; Barbey et al., 2021).

Shell formation

From hand sample and petrographic descriptions, together with *in-situ* mineral composition data, the shells are distinct from both cores and the matrix. Contrary to the coarse-grained cores and matrix, shells are fine-grained and exhibit polygonal textures. In addition to this, the shells are dominated by biotite, magnetite and plagioclase; however, they do not contain hornblende like the cores and matrix (Figures 4 and 5). Although plagioclase shows an almost complete overlap of An contents and $^{87}Sr/^{86}Sr$ isotope ratios in cores, shells and the matrix, considering averages and standard deviations, biotite composition in shells are significantly less magnesian than in cores and the matrix, whose compositions are overlapping. All these characteristics precludes their direct crystallisation from the magma/melt from which the cores and the matrix crystallised, and this probably implies periodic injection of variably evolved magma batches (e.g., McCarthy and Müntener, 2016; Barbey et al., 2021). The presence of magnetite-, plagioclase- and biotite-dominated layers characterising the shells (Figure 4a and b) are evidence of variations in mineralogy, which can be related to the tapping of melt of slightly variable chemistry, temperature, crystal and volatile content, implying that the individual layers represent individual melt pulses (e.g., McCarthy and Müntener, 2016). The differences between these orbicular structures also suggest that processes involving core-matrix formation and shell formation were distinct from one another. The mechanism that formed shells is likely to have involved sudden changes in the physico-chemical environment or conditions of crystallisation in the magma leading to the formation of shells. This is consistent with the sharp contacts observed between cores and shells (e.g., Vernon, 1985), which are interpreted as new melt injections (McCarthy and Müntener, 2016). The main process invoked in numerous studies regarding orbicular rock formation is the fact that the melt is superheated, which leads to resorption of pre-existing crystals or nuclei (Vernon, 1985), followed by undercooling, leading to comb-textured growth of residual solid structures (e.g., wall rock, xenoliths and xenocrysts; Swanson, 1997; Grosse et al., 2010; Ort, 1992) and the growth of orbicules.

Three main mechanisms that trigger superheating have been put forward:

- addition of volatiles into water-undersaturated melt (Vernon, 1985) or;
- adiabatic decompression associated with dykes in zones of pronounced melt extraction (McCarthy and Müntener, 2016; Barbey et al., 2021) or;
- an intrusion of a hotter and more mafic melt (1100 to 1300°C) into a felsic melt (750 to 950°C; Vernon, 1985).

The involvement of a mafic magma would introduce elements such as Fe and Mg, necessary for the formation of mafic minerals (e.g., pyroxenes and olivine). However, Diana's Pool orbicular shells lack such minerals, hence; the involvement of a mafic magma is not conceivable.

We agree that the most popular model to account for superheating is introduction of volatiles (Vernon, 1985; Ort, 1992; Lindh and Näsström 2006; Grosse et al., 2010; Díaz-Alvarado et al., 2017), however, considering the absence of hydrous minerals such as hornblende in shells, this model is not plausible. In addition to this, the addition of volatiles process is very difficult to demonstrate (Lindh and Näsström, 2006) and appears a little bit like a *deus ex machina* (Barbey, pers. comm., 2023). According to Morse (1980), Grove et al. (1992), McCarthy and Müntener (2016) and Barbey et al. (2021), variations in pressure during decompression of magma pulses in dykes play a significant role on the stability of minerals. This would account for the change in the nature of ferromagnesian phases from the cores to the shells and the absence of hornblende in Diana's Pool orbicular shells (Figures 4 and 5). In addition to this, magnetite crystals in the ferromagnesian shells are fine, branched, and comb-layered (radiating-textures), indicating disequilibrium conditions during orbicule crystallisation and rapid growth in a fluid-rich environment (e.g., Lofgren and Donaldson, 1975). According to Smillie and Turnbull (2013), Barbey et al. (2021), Li et al. (2021) and Zhang and Lee (2021), the radiating textures indicate a fast and unimpeded crystal growth in a highly undercooled magma under non-equilibrium conditions. A sudden and important temperature variation is not conceivable in a plutonic environment; hence, the most likely process for rapid supersaturation is volatile exsolution on decompression, displacing liquidus temperature (McCarthy and Müntener, 2016; Barbey et al., 2021).

We thus propose the model invoked first by McCarthy and Müntener (2016) and then by Barbey et al. (2021), considering:

- adiabatic decompression of magma pulses ascending in dykes leading to superheating and resorption of early solids, and
- volatile exsolution, inducing undercooling, supersaturation, and the crystallisation of shells around central cores.

In addition, a third stage is needed to account for deformation of orbicules (removal from the zone of formation).

To form the orbicular shells in the Diana's Pool orbicules, the superheating event triggered by adiabatic decompression of the Matopos granite magma during ascent led to mineral resorption and destruction of nuclei, and this resulted in a decrease in water contents of the ascending melt due to partial resorption of anhydrous crystals. Adiabatic ascent of the melt was then followed by emplacement of the magma in sub-vertical conduits along intra-plutonic contacts (e.g., McCarthy et al., 2016; McCarthy and Müntener, 2016). At this point, degassing occurred as a result of volatile saturation during dyke emplacement and as the melt reached the water-saturated liquidus, heterogeneous nucleation was triggered, and shells started crystallising subsequently on the pre-existing cores (e.g., McCarthy and Müntener, 2016). When the process of shell nucleation around the cores began, it became much faster (e.g., Bevan and Bevan, 2009). This is supported by Grosse et al. (2010), who proposed that the process of orbicule formation is relatively quick and takes about ten days.

All Diana's Pool orbicular shells start with an innermost layer that is rich in plagioclase (Figures 2; 4a and b) and some shells are a succession of plagioclase-dominated or plagioclase- and magnetite-dominated or biotite-dominated layers (Figures 4 and 5). This is an indication that plagioclase was the dominant phase that was crystallising when orbicule growth began, which was then followed by the crystallisation of magnetite- and plagioclase-rich and biotite-rich shells. The alternation and recurrence of these plagioclase-dominated, magnetite-dominated, and biotite-dominated layers can be attributed to oscillatory crystallisation, which is well illustrated by Zhang and Lee (2021), Li et al. (2021), and Barbery et al. (2021). According to these authors, if a cotectic crystallisation of two phases is considered (in this case, plagioclase and magnetite), the onset of crystallisation of both plagioclase and magnetite will result from undercooling. Undercooling is attributed to volatile exsolution from a magma, which drives the liquidus surfaces towards higher temperatures.

The temperature differences between the magma and the liquidus temperature are commensurate with supersaturation, and, for the chosen liquid composition, the degree of plagioclase supersaturation exceeds the degree of magnetite supersaturation, therefore, plagioclase will crystallise in excess compared to magnetite, since the degree of supersaturation is greater for plagioclase. However, excessive crystallisation of plagioclase will cause the residual melt within the crystallising boundary layer to migrate towards the magnetite-rich end-member as it becomes more enriched in magnetite and less enriched in plagioclase components.

The remaining melt preferentially crystallises magnetite when the degree of magnetite supersaturation exceeds the degree of plagioclase supersaturation. The pattern is repeated until the local system returns to plagioclase oversaturation as more cooling occurs, producing these oscillating mafic and felsic shells. The same mechanism can also explain the alternation between these magnetite + plagioclase and biotite-rich layers (Figure 4). Variations in the thickness of shells are also observed (Figures 2b; 3; 4 and 5) and oscillatory crystallisation alone cannot account for this and an additional mechanism is required. It may seem conceivable that periodic injection of more- or less-differentiated melts resulted in this variation (i.e., each layer corresponds to a specific liquid, e.g., Barbey et al., 2021). However, if we consider decompression melting and superheating (inducing crystal-free liquids), significant differentiation during ascent of crustal melts is not possible (e.g., Barbey et al., 2021) and not consistent with the constant composition of plagioclase observed in the different orbicular structures.

Therefore, complementary to oscillatory crystallisation, we propose that fluctuations in the nucleation and growth rates of plagioclase, biotite and magnetite occurred in relation to the degrees of undercooling and supersaturation (e.g., Barbey et al., 2021). Crystal growth can exceed the diffusion rate at significant degrees of undercooling. This will result in a concentration of incompatible elements in front of growing crystals (Mollo and Hammer, 2017). At lower degrees of undercooling, growth rates become slower than the diffusion rate and crystal growth is interface-limited (Mollo and Hammer, 2017).

In the case of Diana's Pool orbicular shell formation (e.g., full orbicular sample BM14780F; Figure 4a and b), rapid plagioclase growth resulted in a thin boundary layer rich in elements that are incompatible with the lattice of plagioclase (Mg and Fe). Supersaturation of these elements promoted the nucleation of magnetite, leading to a thin sheet of small magnetite grains (e.g., magnetite layer in between biotite layers; Figure 4a and b). Conversely, if plagioclase growth is slower, but still faster than diffusion, a less concentrated, more diffuse and thicker boundary layer will result, favouring growth and leading to larger and fewer magnetite crystals (e.g., inner magnetite-rich layer in contact with the core; Figure 4a and b).

We attribute the growth rates of plagioclase, magnetite and biotite to variations in melt supersaturation related to variable volatile exsolution linked to the dynamics of the magma during ascent (e.g., Barbey et al., 2021).

Matrix formation

Prolonged undercooling of the decompressed melt during ascent within the conduit led to homogeneous nucleation, orbicule growth ceased and there was a growth of plagioclase and K-feldspar (micro) phenocrysts (e.g., Blundy and Cashman, 2001), forming the coarse-grained matrix. Judging from the sharp contacts between shells and the matrix, this change must also have been abrupt (e.g., Vernon, 1985; Grosse et al., 2010; Sylvester, 2011). The matrix must have crystallised at a high growth rate, and the grain size increased. The deformation of shells and cores (Figure 2c, d and e; black arrow, Figure 3a) by the granitic matrix material suggests a degree of plasticity within them, suggesting that the early orbicules were deformable but somewhat rigid, and they could move freely in the partially crystallised matrix material (e.g., Ray, 1952). This further suggests that the orbicules continued to evolve in the presence of a melt (matrix material), which possibly dragged them to their present setting (e.g., Ray, 1952; Barbey et al., 2021).

Conclusion

Based on hand sample descriptions, petrological and *in-situ* mineral chemistry data we present here, Diana's Pool orbicules are of magmatic origin that involved two stages:

- adiabatic decompression of melts in dykes or conduits, which led to superheating and resorption of solids, followed by a delay in nucleation and
- volatile exsolution, inducing undercooling, supersaturation, and the crystallisation of shells on existing cores/autoliths, forming orbicules.

At a later stage, orbicule growth ceased and the coarse-grained matrix began to crystallise at high a higher growth, which is consistent with the coarse-grained textures of the matrix. Based on the deformation features they exhibit, the orbicules formed in deeper areas of the crust and were later carried to their present setting possibly by the matrix.

Acknowledgements

The support of the Department of Science and Innovation through its funding agency, the National Research Foundation, and the Centre of Excellence for Integrated Mineral and Energy Resource Analysis (DSI-NRF CIMERA) towards this research is hereby acknowledged. Opinions expressed and conclusions arrived at, are those of the author(s) and are not necessarily to be attributed to the CoE, DSI or NRF. We express our gratitude to Pierre Barbey, Juan Díaz-Alvarado, and Dominique Gasquet for their in-depth reviews, constructive comments and suggestions on our manuscript. We thank the Wits School of Geosciences for providing access to samples. Caiphas Majola and Sam Tshabalala prepared the polished thin sections. Electron microprobe and $^{87}Sr/^{86}Sr$ isotope analyses were performed by Alexander Ziegler (Wits University) and Henriette Ueckermann (University of Johannesburg), respectively. Deshenthree Chetty (Mintek) ran the micro-XRF scanning of samples, and Nonkuselo Madlakana helped with TIMA analyses.

References

Abdel-Rahman, A.F.M., 1994. Nature of biotites from alkaline, calc-alkaline, and peraluminous magmas. Journal of Petrology, 35, 525-541.

Allègre, C.J., Lewin, E. and Dupré, B., 1988. A coherent crust-mantle model for the uranium-thorium-lead isotopic system. Chemical Geology, 70, 211-234.

Amm, F. L., 1940. The geology of the country rocks around Bulawayo. Southern Rhodesia Geological Survey Bulletin 35, 1-307.

Barbey, P., Grandprat, M. and Faure, F., 2021. Cordierite-bearing orbicules record bulk assimilation and the pulsating nature of magma ascent: The Lafaye Orbicular Granite (France). Journal of Petrology, 62, egab063.

Barrière, M., Chauris, L., Cotten, J., 1971. Premières données sur un faciès orbiculaire dans le massif granitique de 1'Aber-Ildut (Finistère, France). Bulletin de Minéralogie, 94, 402.

Bevan, J. and Bevan, A., 2009. Nature and origin of the orbicular granodiorite from Boogardie Station, Western Australia: An ornamental stone of monumental proportions. The Australian Gemmologist, 23, 373-432.

Blundy, J., and Cashman, K., 2001. Ascent-driven crystallization of dacite magmas at Mount St Helens, 1980-1986, Contributions to Mineralogy and Petrology, 140, 631-650, doi: 10.1007/s004100000219.

Bouvier, A., Vervoort, J.D. and Patchett, P.J., 2008. The Lu-Hf and Sm-Nd isotopic composition of CHUR: constraints from unequilibrated chondrites and implications for the bulk composition of terrestrial planets. Earth and Planetary Science Letters, 273, 48-57.

Broderick, T. and Hubbard, P., 2016. The Matobo Hills of Zimbabwe: A perfect blend of geology, scenery and human history. In: Anhaeusser, C. R., Viljoen, M. J., Viljoen, R. P., (eds) 2016. Africa's Top Geological Sites: Struik Nature, Cape Town. 312.

Couturié, J.P., 1973. Un nouveau gisement de granite orbiculaire dans le Massif Central français: le granite du Signal de Randon (Lozère). Contributions to Mineralogy and Petrology, 42, 305-312.

Decitre, S., Gasquet, D. and Marignac, C., 2002. Genesis of orbicular granitic rocks from the Ploumanac'h Plutonic Complex (Brittany, France): petrographical, mineralogical and geochemical constraints. European Journal of Mineralogy, 14, 715-731.

Deer, W., Howie, R., and Zussman, J., 1992. An introduction to the rock-forming minerals. Longman London, UK.

DePaolo, D. and Wasserburg, G., 1976. Inferences about magma sources and mantle structure from variations of $^{143}Nd/^{144}Nd$. Geophysical Research Letters, 3, 743-746.

Díaz-Alvarado, J., Rodríguez, N., Rodríguez, C., Fernández, C. and Constanzo, Í., 2017. Petrology and geochemistry of the orbicular granitoid of Caldera, northern Chile. Models and hypotheses on the formation of radial orbicular textures. Lithos, 284, 327-346.

Durant, D.G. and Fowler, A.D., 2002. Origin of reverse zoning in branching orthopyroxene and acicular plagioclase in orbicular diorite, Fisher Lake, California. Mineralogical Magazine, 66, 1003-1019.

Elburg, M., Vroon, P., van der Wagt, B. and Tchalikian, A., 2005. Sr and Pb isotopic composition of five USGS glasses (BHVO-2G, BIR-1G, BCR-2G, TB-1G, NKT-1G). Chemical Geology, 223, 196-207.

Elliston, J.N., 1984. Orbicules: An indication of the crystallization of hydrosilicates, Earth-Science Reviews, 20, 265-344.

Enz, R.D., Kudo, A.M. and Brookins, D.G., 1979. Igneous origin of the Orbicular Rocks of the Sandia Mountains, New Mexico. Geological Society of America Bulletin, 90, 349-380.

Eskola, P., 1938. On the Esboitic Crystallization of Orbicular Rocks. The Journal of Geology, 46, 448-485.

Faure, G. and Mensing, T.M., 2005. Principles and applications. John Wiley & Sons, Inc.

Garson, M.S., 1995. The geology of the Bulawayo greenstone belt and the surrounding granitic terrain. Zimbabwe Geological Survey. Bulletin (93), 2-94.

Garvie, O. G., 1969. A note on the orbicular granite in the Diana's Pool area, Matopos. Rhodesia. Quarterly News Bulletin, Geological Society of South Africa, 12. No. 4. 11-12.

Garvie, O.G., 1971. Stop 14. Nsezi River. Stop 15. Diana's Pool. In: Excursion Guidebook. Symposium on the granites, gneisses and related rocks. Compiled by E.R. Morrison and J.F. Wilson. Geological Society of South Africa, Rhodesian Branch, 11-14.

Grosse, P., Toselli, A.J. and Rossi, J.N., 2010. Petrology and geochemistry of the orbicular granitoid of Sierra de Velasco (NW Argentina) and implications for the origin of orbicular rocks. Geological Magazine, 147, 451-468.

Grove, T. L., R. J. Kinzler, and Bryan, W. B., 1992. Fractionation of mid-ocean ridge basalt (MORB). In: Mantle flow and melt generation at mid-ocean ridges Gcophys Monogr Am Geophys Union, 71:281-310

Hawkersworth, C.J. and Bickle. M J., I976. Rhodesian Rb-Sr geochronology from 3.8-2.0 b. y., a brief review. 20th Annual. Report, Research Institute African Geology, University of Leeds, 22-27.

Lahti, S.I., 2005. Orbicular Rocks in Finland, with contributions from Paul Raivio and Ilkka Laitakari: Geological Survey of Finland, 177.

Leveson, D.J., 1963. Orbicular Rocks of the Lonesome Mountain Area, Beartooth Mountains, Montana and Wyoming. Geological Society of America Bulletin, 74, 1015.

Leveson, D.J., 1966. Orbicular Rocks: A Review. Geological Society of America Bulletin, 77, 409.

Leveson, D.J., 1973. Origin of Comb Layering and Orbicular Structure, Sierra Nevada Batholith, California: Discussion. Geological Society of America Bulletin, 84, 4005-4006.

Li, Y., Zheng, J. and Satish-Kumar, M., 2021. Combining zircon texture, REE patterns and U-Pb-Hf isotopes to decipher the formation process of orbicular rocks: A case study from Huangling orbicular granodiorite, Yangtze craton, China. Lithos, 386, 106026.

Lindh, A. and Nasstrom, H., 2006. Crystallization of orbicular rocks exemplified by the Slättemossa occurrence, southeastern Sweden. Geological Magazine, 143, 713-722.

Lofgren, G.E. and Donaldson, C.H., 1975. Curved branching crystals and differentiation in comb-layered rocks. Contributions to Mineralogy and Petrology, 49, 309-319.

Makutu, M.N., Kanika, M., Bwanga, N., Nguangu, K., Mpoyi, K., 2004. Petrology and geochemistry of igneous rocks from Noqui Alkaline Complex. Bulletin du Centre de Recherches Géologiques et Minières, 5, 28-39.

McCarthy, A. and Müntener, O., 2016. Comb layering monitors decompressing and fractionating hydrous mafic magmas in subvolcanic plumbing systems (Fisher Lake, Sierra Nevada, USA): Petrology of Fisher Lake Comb Layers. Journal of Geophysical Research: Solid Earth, 121, 8595-8621.

McCarthy, A., Müntener, O., Bouvier, A.S. and Baumgartner, L., 2016. Melt extraction zones in shallow arc plutons: Insights from Fisher Lake orbicules (Sierra Nevada, Western USA). Journal of Petrology, 57, 2011-2052.

Maghdour-Mashhour, R., Hayes, B., Bolhar, R., and Ueckermann, H., 2021. Sill intrusion into pyroxenitic mush and the development of the Lower-Upper Critical Zone boundary of the Bushveld Complex: Implications for the origin of stratiform anorthosites and chromitites in layered intrusions. Journal of Petrology, 62, 1-30.

Mennell, F., 1902. Contributions to South African Petrography. Geological Magazine, 9, 356-366.

Mollo, S., Hammer, J.E., 2017. Dynamic crystallization in magmas. In: Heinrich, W., Abart, R. (Eds.), Mineral Reaction Kinetics: Microstructures, Textures, Chemical and Isotopic Signatures.Mineralogical Society of Great Britain & Ireland, pp. 378-418. https://doi.org/10.1180/EMU-notes.16.12.

Monod, O., Pérez-Segura, E., Richard, D. and Calmus, T., 1995. Orbicular granite sills in the Mazatan core complex, Sonora, Mexico. Revista Mexicana de Ciencias Geologicas, 12, 9-16.

Moore, J.G. and Lockwood, J.P., 1973. Origin of Comb Layering and Orbicular Structure, Sierra Nevada Batholith, California. Geological Society of America Bulletin, 84, 1-20.

Morse, S.A., 1980. Basalts and Phase Diagrams: An Introduction to the Quantitative Use of Phase Diagrams in Igneous Petrology, 493 pp., Springer, New York

Nachit, H., Ibhi, A. and Ohoud, M.B., 2005. Discrimination between primary magmatic biotites, reequilibrated biotites and neoformed biotites. Comptes Rendus Geoscience, 337, 1415-1420

Ort, M.H., 1992. Orbicular volcanic rocks of Cerro Panizos: Their origin and implications for orb formation. Geological Society of America Bulletin, 104, 1048-1058.

Owen, J.V., 1992. Geochemistry of orbicular diorite from the Grenville Front zone, eastern Labrador. Mineralogical Magazine, 56, 451-458.

Palmer, D.F., Bradley, J. and Prebble, W.M., 1967. Orbicular Granodiorite from Taylor Valley, South Victoria Land, Antarctica. Geological Society of America Bulletin, 78, 1423-1428.

Rasbury, E.T., Present, T.M., Northrup, P., Tappero, R.V., Lanzirotti, A., Cole, J.M., Wooton, K.M. and Hatton, K., 2021. Tools for uranium characterization in carbonate samples: case studies of natural U-Pb geochronology reference materials. Geochronology, 3, 103-122.

Ray, R.G., 1952. Orbicular diorite from southern Alaska. American Journal of Science, 250, 57.

Sederholm, J.J., 1928. On orbicular Granites. Geological Society of Finland Bulletin, 83, 80-81.

Sederholm J.J., 1928. On orbicular granites, spotted and nodular granites etc. and on the rapakivi texture. Geological Society of Finland Bulletin, 83,105.

Smillie, R.W. and Turnbull, R.E., 2013. Field and petrographical insight into the formation of orbicular granitoids from the Bonney Pluton, southern Victoria Land, Antarctica. Geological Magazine, 151, 534-549.

Smith, C.G. and Fripp, R.E.P., 1973. The northern contact facies of the Matopos granite, Rhodesia. Geological Society of South Africa Special Publication, 3, 447-53.

Sylvester, A.G., 2011. The nature and polygenetic origin of orbicular granodiorite in the Lower Castle Creek pluton, northern Sierra Nevada batholith, California. Geosphere, 7, 1134-1142.

Symes, R.F., Bevan, J.C. and Qasim Jan, M., 1987. The nature and origin of orbicular rocks from near Deshai, Swat Kohistan, Pakistan. Mineralogical Magazine, 51, 635-647.

Swanson, S.E., 1977. Relation of nucleation and crystal growth rate to the development of granitic textures. American Mineralogist 62, 966-978.

Tagiri, M., Oba, T. and Fujinawa, A., 2007. Radial cordierite-bearing orbicular granite formed from the melting of pelitic hornfels in granitic magma, Tsukuba Mountains, Japan. Journal of Mineralogical and Petrological Sciences, 102, 127-136.

Thompson, T.B. and Giles, D.L., 1974. Orbicular Rocks of the Sandia Mountains, New Mexico. Geological Society of America Bulletin, 85, 911-916.

Vernon, R.H., 1985. Possible role of superheated magma in the formation of orbicular granitoids. Geology, 13, 843-845.

von Buch, F.L., 1802.Geognostische Beobachtungen auf Reisen durch Deutschland und Italien: Berlin, Haude, Band 1, 320.

Workman, R.K. and Hart, S.R., 2005. Major and trace element composition of the depleted MORB mantle (DMM). Earth and Planetary Science Letters, 231, 53-72pp

Zhang, J. and Lee, C.T.A., 2021. Disequilibrium crystallization and rapid crystal growth: a case study of orbicular granitoids of magmatic origin. International Geology Review, 63, 900-916.

Editorial handling: M.A. Elburg.